ACS OMEGA

Open Access

http://pubs.acs.org/journal/acsodf

Article

Low-Temperature Chemical Vapor Deposition Growth of Monolayer MoS_2 Using a Dual-Assisted Approach

Xiangwei Huang,[‖] Kai Liu,[‖] Bojun Shao, Lunchun Guo, Wugang Liao, Congwei Liao,* and Peng Yang*

Cite This: *ACS Omega* 2025, 10, 16257−16264

Read Online

ACCESS | Metrics & More | Article Recommendations

ABSTRACT: The growth of monolayer MoS_2 via chemical vapor deposition typically necessitates high temperatures over 700 °C, which presents challenges for application in the integrated circuit industry where back-end-of-line processes require temperatures possibly below 500 °C. In this study, we demonstrate a method that combines potassium chloride mixed with a MoO_3 precursor and perylene-3,4,9,10-tetracarboxylic acid tetra potassium salt as a seeding promoter for substrate pretreatment, which can effectively lower the growth temperature of MoS_2 on sapphire and SiO_2/Si substrates to 460 °C. The reduced growth temperature is achieved without compromising the material's quality, making this method potentially transformative for the semiconductor industry. Our first-principles calculations and theoretical modeling accurately describe the observed morphological evolution of monolayer MoS_2 crystals during growth. The crystal growth is governed by the probability of atom attachment to different edge types, which is determined by the varying formation energies of the nuclei at these edges. The grown monolayer MoS_2 was characterized through atomic force microscopy, Raman and photoluminescence spectroscopy, and electrical transport measurements, confirming its high quality and suitability for electronic applications.

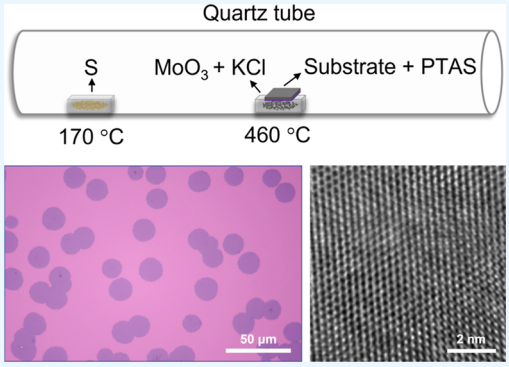

INTRODUCTION

Two-dimensional transition metal dichalcogenide (TMDC) materials have attracted tremendous attention due to their unique optical, electrical, and mechanical characteristics, making them promising candidates for various electronic and optoelectronic applications.[1−8] As a typical TMDC, monolayer MoS_2 is envisioned as a highly promising material for the next-generation electronics and integrated circuits due to its immunity to the short channel effect, ultrathin thickness, high electron mobility, good on/off ratio, and compatibility with semiconductor processes.[1−8] Different methods, such as hydrothermal synthesis, exfoliation, and physical vapor deposition techniques, have been used to synthesize monolayer MoS_2. However, the synthesized MoS_2 layers by these methods are often restricted to either large area uniformity or repeatability, making the synthesis of a large-area MoS_2 thin film challenging. Among different methods, chemical vapor deposition (CVD) has demonstrated great advantages for reproducibly growing large-area, high-quality monolayer MoS_2.[9−11] However, the sublimation of precursor materials and the reactions occurring in the gas phase during CVD necessitate a significant temperature, typically above 700 °C for the synthesis of MoS_2.[9−11] The high temperature is incompatible with the back-end-of-line (BEOL) processes in complementary metal-oxide-semiconductor (CMOS) technologies, which necessitate processing temperatures below 450−600 °C (depending on the process time), where MoS_2 are considered alternative strategies to keep Moore's law alive in the integrated circuit industry.[11−13] Moreover, the high-temperature growth of MoS_2 also hinders its application in flexible electronics, where flexible substrates usually have low melting temperatures.

Several strategies have been employed to reduce the growth temperature of monolayer MoS_2 to comply with the BEOL thermal budget. For instance, wafer-scale monolayer MoS_2 has been grown using metal−organic CVD (MOCVD) at or below 500 °C;[14] however, the growth times are usually longer than 8 h, which limits the throughput. Additionally, the average carrier mobilities reported are generally lower than those for MoS_2 grown at higher temperatures. CVD is still considered an ideal method for preparing monolayer MoS_2 with a high crystal quality and large area feasibility. Therefore, developing CVD techniques that can reduce the growth temperature of monolayer MoS_2 to meet the thermal budget requirements of various electronics applications is highly desirable.

Received: November 13, 2024
Revised: March 13, 2025
Accepted: April 8, 2025
Published: April 16, 2025

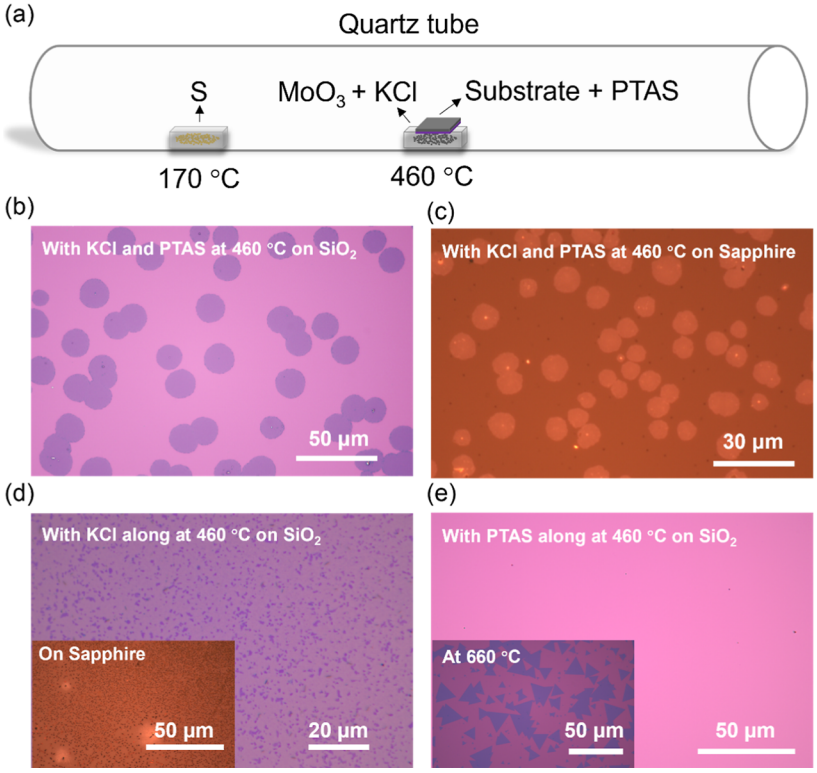

Figure 1. (a) Schematic of the dual-assisted growth of MoS_2. Optical image of MoS_2 layers grown on SiO_2 (b) and sapphire (c) with the dual-assisted approach. (d) Typical growth results obtained with only KCl at 460 °C on SiO_2 and sapphire (inset); only MoS_2 particles are formed. (e) Typical growth results obtained with only the PTAS seeding promoter at 460 and 660 °C (inset) on a SiO_2 substrate. At 460 °C, the MoS_2 failed to nucleate, and nothing can be found on the substrate; only when the temperature is raised to around 660 °C, the typical triangular MoS_2 flakes start to form.

Recent advancements have demonstrated the possibility of reducing the growth temperature of MoS_2 while maintaining crystalline quality using CVD methods.[15−25] As discussed, the primary reason for the high-temperature growth of MoS_2 is the high melting point and low vapor pressure of the commonly used metal oxide precursor, MoO_3. Therefore, one approach to lower the growth temperature is to use more volatile precursors. By using $(NH_4)_2MoO_4$ (AHM) as the Mo source precursor, Gong et al. successfully obtained monolayer MoS_2 on a polyimide (PI) substrate at 450 °C.[22] Additionally, it has been found that incorporating tellurium (Te) as a growth intermediate can reduce the growth temperature of MoS_2; Gong et al. successfully grew monolayer MoS_2 single crystals at 500 °C by mixing tellurium (Te) powder with MoO_3.[23] However, recent studies have shown that MoS_2 flakes grown using MoO_3 and sulfur (S) precursors exhibit better uniformity, crystallinity, and reproducibility compared to those grown using AHM and Te-assisted methods.[26] Thus, methods that reduce the growth temperature of MoS_2 while using MoO_3 and S precursors remain desirable. It has been reported that the use of alkali halides, such as NaCl and KCl, can facilitate the reaction during the growth process with MoO_3 and S, effectively reducing the synthesis temperature to 650 °C and producing high-quality few-layer MoS_2.[15−20] Moreover, studies have shown that pretreating the substrate with seeding promoters, such as perylene-3,4,9,10-tetracarboxylic acid tetra potassium salt (PTAS), can enhance the nucleation and growth of MoS_2 on substrates at lower temperatures,[27,28] although this approach has not yet achieved growth temperatures below 500 °C. This study investigates the combined effect of KCl salt and the PTAS seeding promoter in lowering the growth temperature of MoS_2 to 460 °C without compromising material quality, a temperature compatible with the back-end processing requirements in semiconductor manufacturing. Raman spectroscopy, photoluminescence (PL), atomic force microscopy (AFM), and high-resolution transmission electron microscopy (HRTEM) were used to confirm the uniform thickness, stoichiometry, and lattice spacing of the MoS_2 layers.

EXPERIMENTAL SECTION

A silicon wafer with 300 nm of wet-oxidized SiO_2 and a *c*-plane sapphire were used as the growth substrates in the experiments. Before the deposition, these substrates were ultrasonically cleaned in acetone, followed by rinses in demineralized water and isopropanol, each for 20 min. Subsequently, the substrates were dried by using nitrogen gas. After that, the substrates were treated with a 100 μM solution of the organic seeding promoter PTAS and then air-dried naturally.

The schematic for the CVD growth of MoS_2 is shown in Figure 1a. A two-temperature-zone furnace with a 2 in. quartz tube was used for the growth of monolayer MoS_2. Two quartz boats of 5 mg of MoO_3 (Aladdin 99.9%) mixed with 1 mg of KCl and 120 mg of sublimed sulfur (Aladdin 99.99%) were positioned in the two heating zones, respectively. The substrates pretreated with PTAS were placed face down on top of the quartz boat with MoO_3 and KCl. The distance between the two heating zones was 22 cm. The quartz chamber was first pumped down to 1 Pa for 30 min to eliminate air contamination. After that, the two temperature

https://doi.org/10.1021/acsomega.4c10312
ACS Omega 2025, 10, 16257−16264

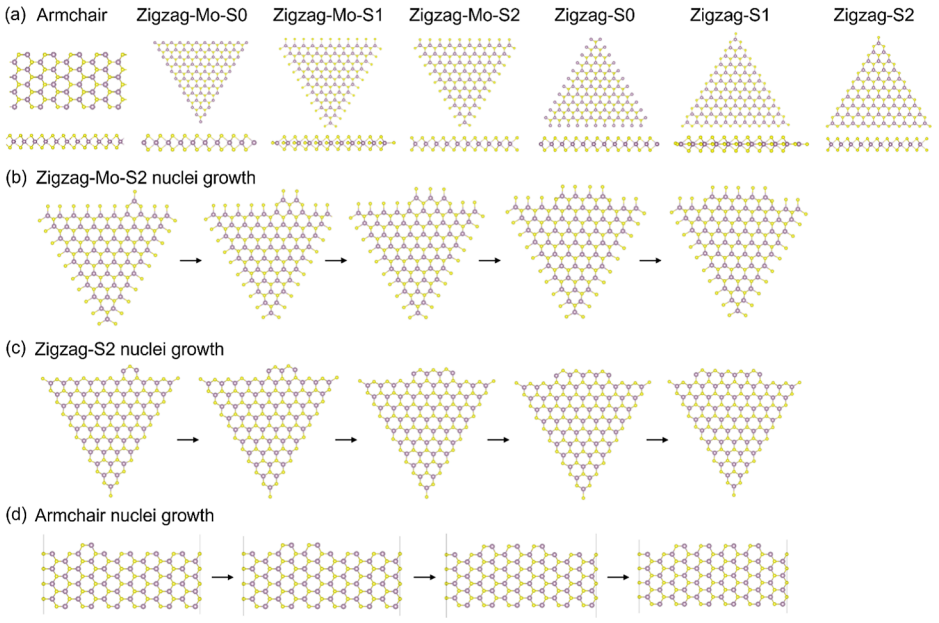

Figure 2. (a) Top view (upper) and side view (lower) of seven possible edge configurations during the growth stage of the hexagonal MoS_2 crystal. (b–d) Atomistic modeling of the growth behavior of single-crystal MoS_2 domains. The edge structures of hexagonal domains, including (b) zigzag-Mo-S_2, (c) zigzag-S_2, and (d) armchair edges, were optimized with the addition of nuclei. The nucleus configurations exhibit tilted edges, with tilting angles of approximately 19° relative to the zigzag edges.

zones were raised to 170 and 460 °C, respectively, within 30 min and were stabilized at these temperatures for 10 min to grow MoS_2.

During the growth, the chamber was kept at atmospheric pressure with a N_2 carrier gas with a flow rate of 10 sccm. Finally, the furnace was naturally cooled down to room temperature. In most salt-assisted growth studies of monolayer MoS_2, NaCl is typically mixed with MoO_3. However, in our dual-assisted growth strategy, we found KCl is superior to NaCl for growing monolayer MoS_2 with uniform topography, consistent with a recent study showing that K^+ has a greater promoting effect than Na^+ in MoS_2 growth.[29]

The morphologies of the grown MoS_2 layers were characterized by optical microscopy (Nikon ECLIPSE LV100ND). The height of the synthesized sample was measured by atomic force microscopy (AFM) (Bruker Dimension Icon with ScanAsyst). The formation energies of MoS_2 edges were investigated using first-principles calculations. For hexagonal MoS_2, the crystalline symmetry gives rise to several distinct edge types: armchair (AC), Mo-terminated zigzag (ZZ)—including ZZ-Mo-S_0, ZZ-Mo-S_1, and ZZ-Mo-S_2—and S-terminated zigzag—including ZZ-S_0, ZZ-S_1, and ZZ-S_2, as depicted in Figure 2a. To mitigate spurious interactions between the top and bottom surfaces resulting from the periodic supercell, a vacuum region of approximately 20 Å and dipole moment corrections were applied. To accurately predict the experimental growth dynamics, thermal corrections incorporating the temperature and partial pressure conditions of the reaction were implemented through an analysis of the vibrational modes of the reactants. The edge growth behavior of MoS_2 was also modeled considering three potential growth patterns. The structural evolution of these patterns is illustrated in Figure 2b–d. Raman and Photoluminescence (PL) spectra were measured using a WITec Alpha 300R system at room temperature, and the excitation laser wavelength was 532 nm. The Raman peak of a silicon wafer at 520 cm^{-1} was used as the reference to calibrate the spectrometer. High-resolution transmission electron microscopy (HRTEM) images were obtained using a JEOL-F200 TEM. The electrical transport properties of the MoS_2 field-effect transistor (FET) were measured at room temperature using an Agilent Technologies B1500A semiconductor device analyzer.

RESULTS AND DISCUSSION

Figure 1b–c shows the typical optical microscopy image of the as-grown MoS_2 layers, which are distributed homogeneously on the substrate. The as-grown MoS_2 exhibited a round shape with dimensions of approximately 10–20 μm. These round-shaped MoS_2 layers differ from the commonly observed triangle-shaped MoS_2. Previous studies indicate that under thermodynamic equilibrium, the triangle shape is the stable state due to the hexagonal symmetry of MoS_2. However, when the growth rate is high, the process shifts to a kinetically controlled regime, leading to the formation of round-shaped MoS_2. This suggests that higher temperatures favor the formation of round shapes.[30] The round shape of monolayer MoS_2 can also be attributed to specific growth conditions and controlled synthesis techniques that influence the chemical potential and nucleation dynamics during the growth process.[30−32]

To understand the role of the two promoters in the dual-assisted approach, comparison experiments were conducted using only KCl salt and the PTAS seeding promoter at 460 °C to grow MoS_2. As depicted in Figure 1b–e, with KCl along, only MoS_2 particles were deposited on the substrates, aligning with the findings reported by Kong et al.[27] However, with only PTAS, no film was formed on the substrate due to the lack of volatile molybdenum. It is to note that, at a higher temperature of around 660 °C, MoS_2 flakes can be grown using only PTAS. These experiments indicate that KCl and PTAS play distinct roles in facilitating the low-temperature growth of MoS_2. KCl

https://doi.org/10.1021/acsomega.4c10312
ACS Omega 2025, 10, 16257−16264

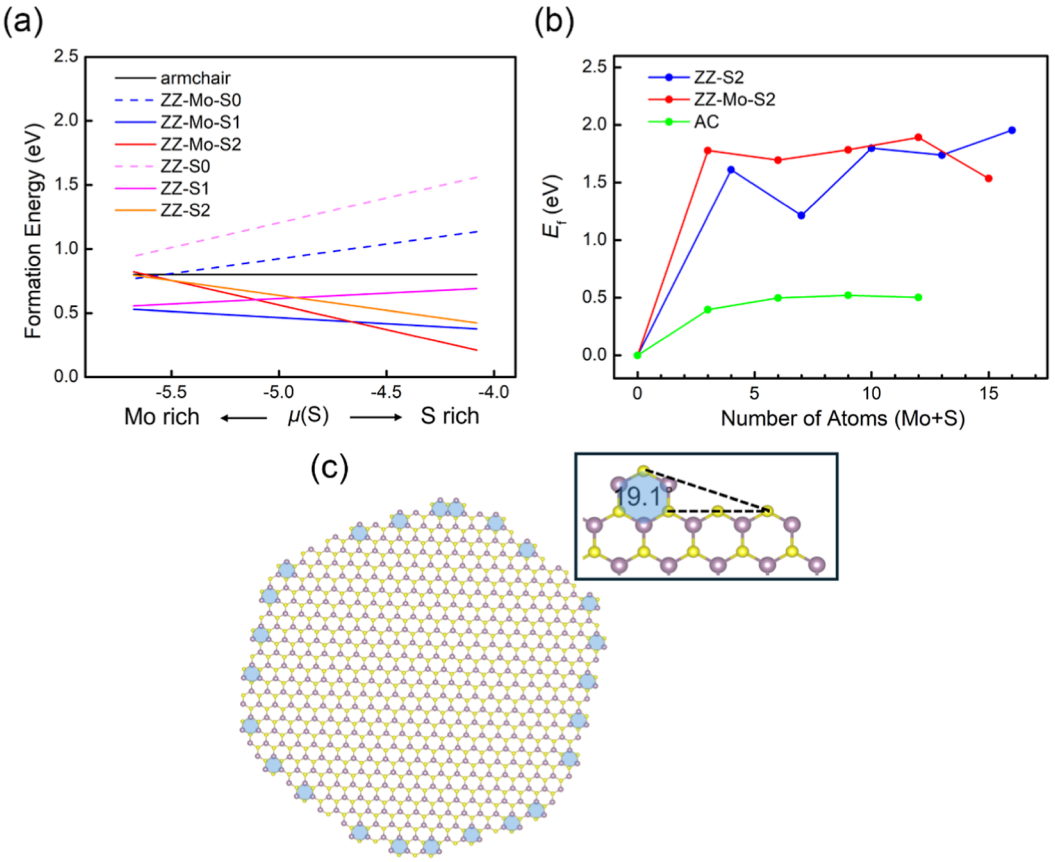

Figure 3. (a) The formation energy of MoS_2 edges with different terminations and S coverages. (b) Free-energy (E_f) evolution during MoS_2 edge growth in ZZ and AC edges: (blue solid line) ZZ-S_2, (red solid line) ZZ-Mo-S_2, and (green solid line) AC edges. (c) Schematic representation of dodecagon-shaped MoS_2 crystals. The inset illustrates the formation of kinks at zigzag edges, characterized by a tilting angle of 19.1°.

is crucial for reducing the melting point of MoO_3 and thus promoting its volatilization; monolayer MoS_2 fails to nucleate at low temperatures without adding KCl. The seeding promoter PTAS is for lowering the surface energy required for MoS_2 formation, thus enabling the formation of a homogeneous film even at the relatively low temperature of 460 °C. We theoretically modeled the morphologies of MoS_2 flakes, which can be determined by either the edge energies at equilibrium or by nonequilibrium growth kinetics at the edges. First, we consider the equilibrium shape of the monolayer MoS_2 domains. The formation energies of these edges were calculated as a function of the sulfur chemical potential, as shown in Figure 3a. Our ab initio thermodynamic analysis indicates that the sulfur chemical potential is close to the S-rich limit due to the high volatility of sulfur vapor. Under such conditions, the ZZ-Mo edge with full sulfur coverage (ZZ-Mo-S_2, represented by the red solid line) is the most stable configuration, with a formation energy approximately 0.2 eV lower than that of the opposite domain orientation (ZZ-S_2, represented by the orange solid line). Although triangular monolayer domains are occasionally observed, a majority of our as-grown flakes exhibit round shapes, which are not predicted by equilibrium edge energy calculations.

Therefore, we further consider the growth kinetics at the edges. During the growth process, according to the kinetic Wulff construction (KWC) theory,[31−33] the growth of a straight AC/ZZ edge must be initiated by the formation of a nucleus. Edges that grow rapidly become smaller, and ultimately, only the slowest-growing edges remain. The results, shown in Figure 3b, indicate that the calculated formation energies of the ZZ-S_2 and ZZ-Mo-S_2 nuclei on MoS_2 edges are 2.01 and 1.77 eV, respectively. In comparison, the initial nucleation energy of the AC edge is only 0.39 eV, consistent with previous analyses. Given the larger barrier for nucleation initiation, the growth rate of both ZZ edges must be slower than that of the AC edge. Consequently, this results in a dodecagonal morphology, terminated with 12 edges tilted by 19.1° relative to the zigzag edges, which are close to the round shape as observed in our samples. We propose that a decrease in growth temperature, along with the use of PTAS seeding promoters, contributes to both a higher growth rate of ZZ edges and ZZ nucleus formation energies, potentially increasing the kink formation rate of MoS_2 along the ZZ edges. The proposed schematic representation of such a dodecagonal-shaped MoS_2 is provided in Figure 3c.

Figure 4 shows a representative atomic force microscopy (AFM) topographic image of the as-grown round MoS_2 layer; the cross-sectional profile (Figure 4b) depicts a thickness of about 0.8 nm, corresponding to a monolayer MoS_2 sample. The crystal quality and phase purity of the MoS_2 monolayer were further evaluated using high-resolution transmission electron microscopy (HRTEM) as shown in Figure 5. The selected area electron diffraction (SAED) pattern (Figure 5a) consisted of one set of diffraction spots with the closest to the central beam arranged in a hexagonal configuration, confirming the single-crystalline characteristic of the grown MoS_2 monolayer. The indexing of the electron diffraction spots revealed the layer's orientation along the [001] zone axis. The

https://doi.org/10.1021/acsomega.4c10312
ACS Omega 2025, 10, 16257−16264

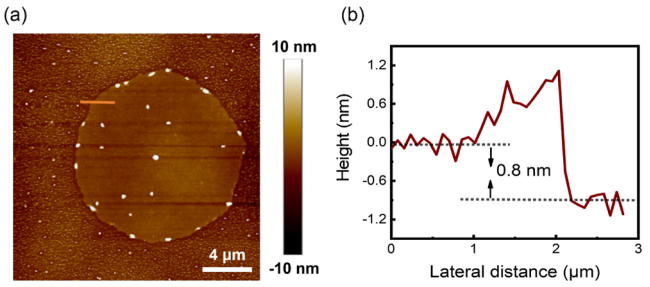

Figure 4. (a) AFM image of a grown MoS_2 layer on the SiO_2/Si substrate. (b) The height profile corresponding to the orange line across the sample in (a) shows a thickness of 0.8 nm.

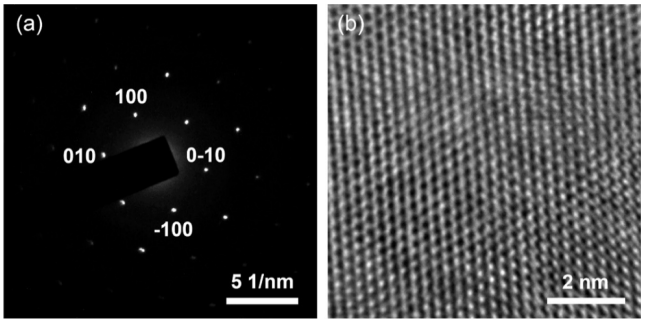

Figure 5. (a) SAED pattern enlightening the single-crystal nature of the grown MoS_2 monolayer. (b) HRTEM image of the MoS_2 sample showing a hexagonal structure.

high-resolution TEM image (Figure 5b) shows a crystal lattice composed of hexagonal rings, revealing a lattice spacing of 3.2 Å and confirming the 2H phase composition as a hexagonal MoS_2.

Raman spectroscopy was performed to further determine the layer number of the grown MoS_2 layer. Figure 6a shows the Raman spectrum obtained from the as-grown MoS_2 sample with two dominant peaks located at 384.0 cm^{-1} and 404.0 cm^{-1}, respectively. They are named E_{2g}^1 and A_{1g} modes, representing the in-plane and out-of-plane vibration of Mo−S. The frequency difference of the two characteristic peaks is 20.0 cm^{-1} in the spectrum, which is a signature of the monolayer MoS_2.[14−30] Figure 6b−d shows the Raman intensity mappings of A_{1g} and E_{2g}^1 and their position difference of the grown monolayer. All of the mappings exhibit a uniform distribution, with the exception of a small dot at the center of the monolayer, which may be due to a contaminant or the presence of multilayer MoS_2 at the central nucleation site. These mappings indicate excellent spatial uniformity of the grown monolayer MoS_2 on the SiO_2/Si substrate.

Figure 7 shows the PL spectrum of MoS_2 along with a spatially resolved mapping image of a typical crystalline domain. The PL peaks of MoS_2 were deconvoluted into three components, corresponding to the A^--exciton, A-exciton, and B-exciton peaks, with peak positions at 1.82, 1.85, and 1.97 eV, respectively. In monolayer MoS_2, the conduction band minimum (CBM) and valence band maximum (VBM) are located at the *K* and *K*′ points of the Brillouin zone. Due to the hybridization of Mo d-orbitals and S p-orbitals, the valence band splits into two subbands at the *K* point under spin−orbit coupling (SOC).[34,35] The A-exciton corresponds to the lower-energy transition, while the B-exciton arises from the higher-energy transition. When additional free carriers (e.g., electrons or holes) are present in MoS_2, neutral excitons can bind with

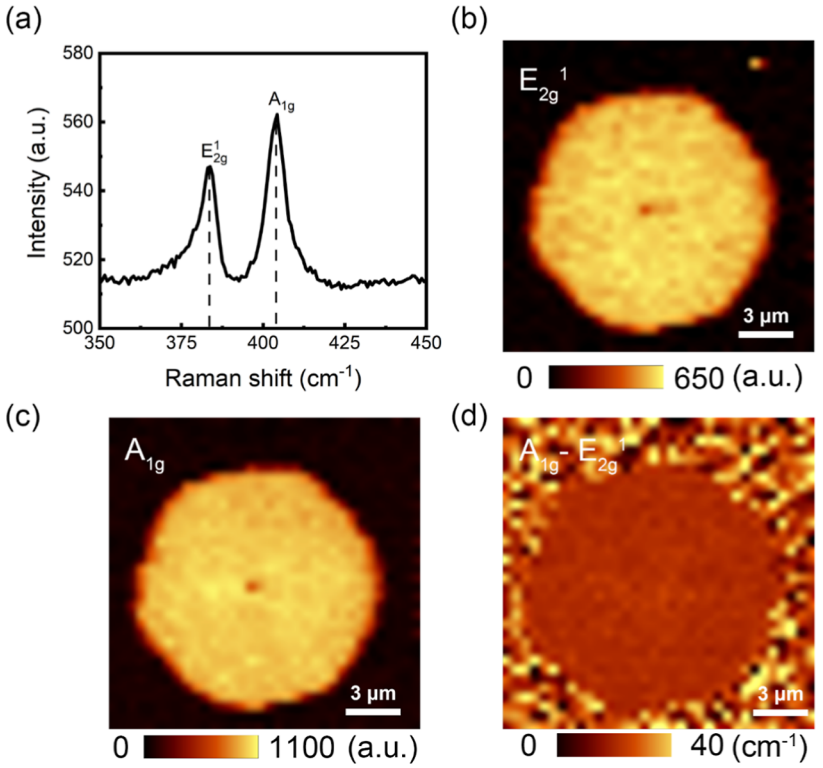

Figure 6. Raman spectrum (a) and intensity mapping of E_{2g}^1 and A_{1g} modes and their position difference (b−d) obtained from a MoS_2 monolayer, respectively.

https://doi.org/10.1021/acsomega.4c10312
ACS Omega 2025, 10, 16257−16264

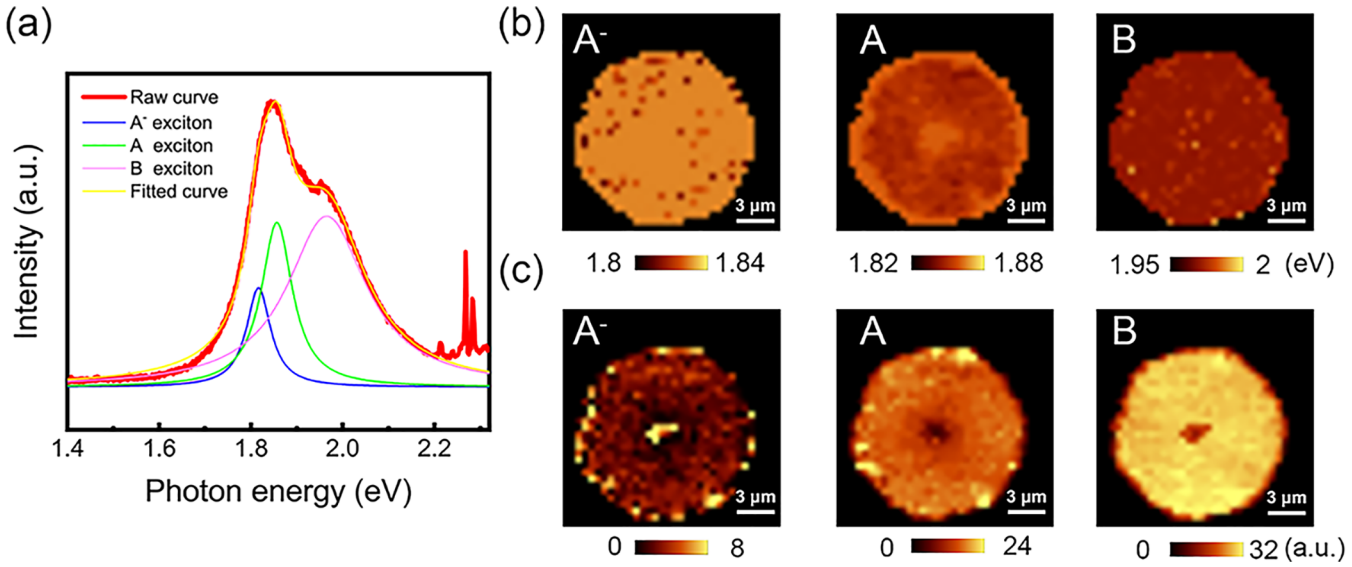

Figure 7. (a) Normalized PL spectrum, position spatial mapping (b), and intensity mapping (c) of the deconvoluted data obtained from a MoS_2 monolayer.

these carriers to form charged excitons (trions), i.e., the A^--exciton.[36] The peak positions and intensity mapping of the three peaks are shown in Figure 7b,c. The peak positions exhibit minimal shifts, all within the range reported in the literature.[35,36] However, the PL intensities of all three peaks show significant attenuation at the center of the MoS_2 domain. This weakening may stem from the presence of a contaminant or multilayer MoS_2 at the central nucleation site, where the indirect bandgap suppresses PL emission.

A typical XPS spectrum of MoS_2 was used to measure binding energies of Mo and S atoms as shown in Figure 8. The

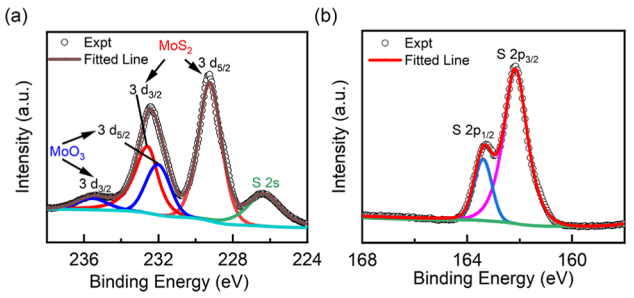

Figure 8. XPS spectra of MoS_2 showing the doublet Mo 3d (a) and S 2s (b) peaks.

Mo 3d peaks at 229.3 and 232.5 eV exhibit the oxidation state of Mo^{4+} due to a doublet caused by $l-s$ coupling. S 2p also shows a doublet of S $2p_{3/2}$ and S $2p_{1/2}$ peaks with binding energies of 162.2 and 163.5 eV, respectively. The two doublets obtained show the successful synthesis of MoS_2. The presence of peaks at 232.2 and 235.4 eV shows the presence of MoO_3 during the formation of MoS_2.

To evaluate the electrical properties of the as-grown monolayer MoS_2, FET devices were fabricated using standard lithography processes. Two Cr/Au electrical contacts were deposited on the MoS_2 monolayer to serve as the source and drain, with the heavily doped silicon substrate functioning as the bottom gate. The inset of Figure 9a shows an optical image of a typical device. The output and transfer curves of this device are displayed in Figure 9a,b. As shown in Figure 9a, the

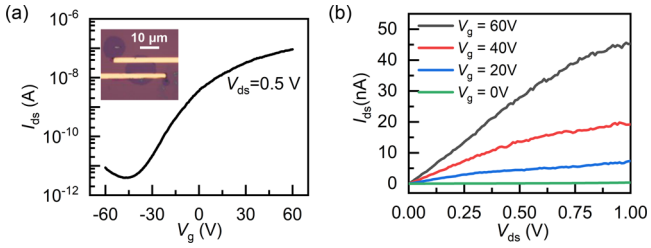

Figure 9. Electrical characteristics of MoS_2 FET. (a) Transfer curve of the monolayer MoS_2-based FET device; the inset is the optical image of the corresponding device. (b) Output curves for the FET device.

MoS_2 FET exhibits n-type semiconducting behavior, similar to that observed in mechanically exfoliated monolayer MoS_2 and other CVD-grown MoS_2 samples.[21−33] The field-effect mobility of the MoS_2 device was calculated by using the following formula

$$\mu = \frac{L}{W \times C_g \times V_{ds}} \times \frac{dI_{ds}}{dV_g}$$

L and W represent the channel length and width, respectively, and C_g is the capacitance (C_g = 1.15 × 10^{-8} F/cm^2) for 300 nm SiO_2.

The typical FET device exhibits an on/off ratio of approximately 10^5, which is relatively lower than previously reported values for high-quality, CVD-grown, triangle-shaped MoS_2.[21−33] The field effect mobility (μ) was extracted from the linear regime of the transfer curve, showing a value of approximately 0.26 $cm^2/(V\ s)$ at room temperature, which is within the range of other reported CVD-grown monolayer MoS_2.[21−33] Interestingly, a similar on/off ratio has been observed in other studies involving round-shaped MoS_2 layers.[30] This lower on/off ratio may be attributed to midgap states present in the round-shaped MoS_2 layers, as speculated in this study.

In Table 1, we compare various CVD-grown methods below 500 °C previously reported in the literature. These methods include the use of more volatile or reactive precursors, such as $(NH_4)_2MoO_4$[22] and MoO_2Cl_2,[38] or mixing Te in the

https://doi.org/10.1021/acsomega.4c10312
ACS Omega 2025, 10, 16257−16264

Table 1. Low-Temperature Monolayer MoS_2 Growth Methods below 500 °C from the Literature

Growth method	growth temperature (°C)	growth time (min)	FET mobility ($cm^2/(V\ s)$)	on/off ratio	reference
$(NH_4)_2MoO_4$ precursor	450	10	-	-	22
MoO_2Cl_2 precursor	360	30	14.3	10^5	38
Te assisted	500	15	4.5	10^5	23
pattern stimulated	500	60	-	-	37
KCl and PTAS	460	10	0.26	10^5	this work

precursor.[23] However, the quality of the grown samples is reported to be inferior to that of those grown using a solid source.[26] Xu et al. also achieved the growth of MoS_2 monolayers at 500 °C by transferring a paste of MoS_2 powder, $Na_2S_2O_3$ powder, and H_2O onto a PDMS pattern.[37] However, the complicated precursor transfer process involved is generally not suitable for mass production. The method presented in this paper, utilizing a solid source to directly grow MoS_2 monolayers on different substrates, demonstrates a significant thermal budget advantage, considering both the growth temperature and time.

CONCLUSIONS

In conclusion, the dual-assisted approach demonstrated in this study successfully reduced the growth temperature of monolayer MoS_2 on a SiO_2/Si substrate to 460 °C without compromising material quality, as confirmed by extensive characterization techniques. The combined use of KCl with MoO_3 and PTAS as seeding promoters played a crucial role in lowering the melting temperature of the MoO_3 precursor and the energy barrier for nucleation and growth, resulting in the formation of round-shaped as-grown layers, as demonstrated by our first-principles calculations. Additionally, the round shape of the MoS_2 layers indicates a kinetically controlled growth process under our specific experimental conditions, which could be further optimized for various applications. This reduction in growth temperature is vital for integrating MoS_2 into semiconductor processes, where high temperatures could damage other device components. The cost-effective and scalable method presented in this study may have potential applications that require high-quality MoS_2 films with a low thermal budget. However, we also need to point out that reducing the growth temperature of MoS_2 is only one of the challenges in applying this material to the semiconductor industry. Other challenges include controllable growth of wafer-size samples, controlling the thickness and quality of the samples, realizing high-performance P and N-type complementary devices, as well as the development of precise 2D material simulation tools, and the development of monolithic 3D integration processes for 2D materials. Only by continuing to develop these aspects can we potentially drive 2D materials into the next generation of information technology and emerging industries.

AUTHOR INFORMATION

Corresponding Authors

Congwei Liao − *College of Integrated Circuits and Optoelectronic Chips, Shenzhen Technology University, Shenzhen 518118, China*; Email: liaocongwei@sztu.edu.cn

Peng Yang − *College of Integrated Circuits and Optoelectronic Chips, Shenzhen Technology University, Shenzhen 518118, China*; Email: yangpeng@sztu.edu.cn

Authors

Xiangwei Huang − *College of Integrated Circuits and Optoelectronic Chips, Shenzhen Technology University, Shenzhen 518118, China; Faculty of Marine Science and Technology, Beijing Institute of Technology, Zhuhai 519088, China*; orcid.org/0000-0003-3803-1390

Kai Liu − *College of Integrated Circuits and Optoelectronic Chips, Shenzhen Technology University, Shenzhen 518118, China*

Bojun Shao − *College of Integrated Circuits and Optoelectronic Chips, Shenzhen Technology University, Shenzhen 518118, China*

Lunchun Guo − *College of Integrated Circuits and Optoelectronic Chips, Shenzhen Technology University, Shenzhen 518118, China*

Wugang Liao − *State Key Laboratory of Radio Frequency Heterogeneous Integration, College of Electronics and Information Engineering, Shenzhen University, Shenzhen 518060, China*; orcid.org/0000-0002-1461-2222

Complete contact information is available at: https://pubs.acs.org/10.1021/acsomega.4c10312

Author Contributions

[‖]X.H. and K.L. contributed equally to this work. P. Y. and C. L. conceived and designed the experiments, P. Y., X. H., and B. S. carried out the experiments, K. L. performed the DFT simulation and calculation, P. Y., C. L., X. H., L. G., and K. L. analyzed the data and discussed the results. X. H., K. L., and B. S. cowrote the manuscript. P. Y., W. L., L. G., and C. L. revised the manuscript. All authors have read and commented on the manuscript.

Notes

The authors declare no competing financial interest.

ACKNOWLEDGMENTS

This research was funded by the National Natural Science Foundation of China (Grant No. 62404138), the Shenzhen Science and Technology Program (Grant No. 20231128102926002), Natural Science Foundation of Top Talent of SZTU (Grant no. GDRC202420), and Pingshan District Innovation Platform Project of Shenzhen Hi-tech Zone Development Special Plan in 2022 (29853M-KCJ-2023-002-01). W.L. thanks the financial support from the Guangdong Basic and Applied Basic Research Foundation (Grant No. 2023A1515010693), the Shenzhen University 2035 Program for Excellent Research (2023C008).

REFERENCES

(1) Radisavljevic, B.; Radenovic, A.; Brivio, J.; Giacometti, V.; Kis, A. Single-layer MoS_2 transistors. *Nat. Nanotechnol.* **2011**, *6*, 147−150.

(2) Huo, Z.; Wei, Y.; Wang, Y.; Wang, Z. L.; Sun, Q. Integrated self-powered sensors based on 2D material devices. *Adv. Funct. Mater.* **2022**, *32*, 2206900.

(3) Daus, A.; Vaziri, S.; Chen, V.; Köroğlu, Ç.; Grady, R. W.; Bailey, C. S.; Lee, H. R.; Schauble, K.; Brenner, K.; Pop, E. High-performance flexible nanoscale transistors based on transition metal dichalcogenides. *Nat. Electron.* **2021**, *4*, 495−501.
(4) Zha, J.; Luo, M.; Ye, M.; Ahmed, T.; Yu, X.; Lien, D.-H.; He, Q.; Lei, D.; Ho, J. C.; Bullock, J.; Crozier, K. B.; Tan, C. Infrared photodetectors based on 2D materials and nanophotonics. *Adv. Funct. Mater.* **2022**, *32*, 2111970.
(5) Tan, C.; Cao, X.; Wu, X.-J.; He, Q.; Yang, J.; Zhang, X.; Chen, J.; Zhao, W.; Han, S.; Nam, G.-H.; Sindoro, M.; Zhang, H. Recent advances in ultrathin two-dimensional nanomaterials. *Chem. Rev.* **2017**, *117*, 6225−6331.
(6) Tan, C.; Zhang, H. Two-dimensional transition metal dichalcogenide nanosheet-based composites. *Chem. Soc. Rev.* **2015**, *44*, 2713−2731.
(7) Ye, Z.; Tan, C.; Huang, X.; Ouyang, Y.; Yang, L.; Wang, Z.; Dong, M. Emerging MoS_2 Wafer-Scale Technique for Integrated Circuits. *Nano-Micro Lett.* **2023**, *15*, 38.
(8) Zhou, J.; Lin, J.; Sims, H.; Jiang, C.; Cong, C.; Brehm, J. A.; Zhang, Z.; Niu, L.; Chen, Y.; Zhou, Y.; Wang, Y.; Liu, F.; Zhu, C.; Yu, T.; Suenaga, K.; Mishra, R.; Pantelides, S. T.; Zhu, Z.-G.; Gao, W.; Liu, Z.; Zhou, W. Synthesis of co-doped MoS_2 monolayers with enhanced valley splitting. *Adv. Mater.* **2020**, *32*, 1906536.
(9) Lan, S.; Zhang, Z.; Hong, Y.; She, Y.; Pan, B.; Xu, Y.; Wang, P. Judicious selection of precursors with suitable chemical valence state for controlled growth of transition metal chalcogenides. *Adv. Mater. Interfaces* **2023**, *10*, 2300713.
(10) Yu, J.; Li, J.; Zhang, W.; Chang, H. Synthesis of High-quality two-dimensional materials via chemical vapor deposition. *Chem. Sci.* **2015**, *6*, 6705−6716.
(11) Zhang, X.; Lai, J.; Gray, T. Recent progress in low-temperature CVD growth of 2D materials. *Oxford Open Mater. Sci.* **2023**, *3*, itad010.
(12) Zhu, K.; Wen, C.; Aljarb, A. A.; Xue, F.; Xu, X.; Tung, V.; Zhang, X.; Alshareef, H. N.; Lanza, M. The development of integrated circuits based on two-dimensional materials. *Nat. Electron.* **2021**, *4*, 775−785.
(13) Wang, S.; Liu, X.; Xu, M.; Liu, L.; Yang, D.; Zhou, P. Two-dimensional devices and integration towards the silicon lines. *Nat. Mater.* **2022**, *21*, 1225−1239.
(14) Mun, J.; Park, H.; Park, J.; Joung, D.; Lee, S.-K.; Leem, J.; Myoung, J.-M.; Park, J.; Jeong, S.-H.; Chegal, W.; Nam, S.; Kang, S.-W. High-mobility MoS_2 directly grown on polymer substrate with kinetics-controlled metal-organic chemical vapor deposition. *ACS Appl. Electron. Mater.* **2019**, *1*, 608−616.
(15) Singh, A.; Moun, M.; Sharma, M.; Barman, A.; Kumar Kapoor, A.; Singh, R. NaCl-assisted substrate dependent 2D planar nucleated growth of MoS_2. *Appl. Surf. Sci.* **2021**, *538*, 148201.
(16) Li, S. Salt-assisted chemical vapor deposition of two-dimensional transition metal dichalcogenides. *iScience* **2021**, *24*, 103229.
(17) Huang, L.; Hu, Z.; Jin, H.; Wu, J.; Liu, K.; Xu, Z.; Wan, J.; Zhou, H.; Duan, J.; Hu, B.; Zhou, J. Salt-assisted synthesis of 2D materials. *Adv. Funct. Mater.* **2020**, *30*, 1908486.
(18) Zhou, J.; Lin, J.; Huang, X.; Zhou, Y.; Chen, Y.; Xia, J.; Wang, H.; Xie, Y.; Yu, H.; Lei, J.; Wu, D.; Liu, F.; Fu, Q.; Zeng, Q.; Hsu, C.-H.; Yang, C.; Lu, L.; Yu, T.; Shen, Z.; Lin, H.; Yakobson, B. I.; Liu, Q.; Suenaga, K.; Liu, G.; Liu, Z. A library of atomically thin metal chalcogenides. *Nature* **2018**, *556*, 355−359.
(19) Khan, U.; Nairan, A.; Khan, K.; Li, S.; Liu, B.; Gao, J. Salt-assisted low-temperature growth of 2D Bi_2O_2Se with controlled thickness for electronics. *Small* **2023**, *19*, 2206648.
(20) Ji, Q.; Su, C.; Mao, N.; Tian, X.; Idrobo, J. C.; Miao, J.; Tisdale, W. A.; Zettl, A.; Li, J.; Kong, J. Revealing the Brønsted-Evans-Polanyi relationin halide-activated fast MoS_2 growth toward millimeter-sized 2D crystals. *Sci. Adv.* **2021**, *7*, No. eabj3274.
(21) Qin, B.; Saeed, M. Z.; Li, Q.; Zhu, M.; Feng, Y.; Zhou, Z.; Fang, J.; Hossain, M.; Zhang, Z.; Zhou, Y.; Huangfu, Y.; Song, R.; Tang, J.; Li, B.; Liu, J.; Wang, D.; He, K.; Zhang, H.; Wu, R.; Zhao, B.; Li, J.; Liao, L.; Wei, Z.; Li, B.; Duan, X.; Duan, X. General low-temperature growth of two-dimensional nanosheets from layered and nonlayered materials. *Nat. Commun.* **2023**, *14*, 304.
(22) Gong, Y.; Li, B.; Ye, G.; Yang, S.; Zou, X.; Lei, S.; Jin, Z.; Bianco, E.; Vinod, S.; Yakobson, B. I.; Lou, J.; Vajtai, R.; Zhou, W.; Ajayan, P. M. Direct growth of MoS_2 single crystals on polyimide substrates. *2D Mater.* **2017**, *4*, 021028.
(23) Gong, Y.; Lin, Z.; Ye, G.; Shi, G.; Feng, S.; Lei, Y.; Elias, A. L.; Perea-Lopez, N.; Vajtai, R.; Terrones, H.; Liu, Z.; Terrones, M.; Ajayan, P. M. Tellurium-assisted low-temperature synthesis of MoS_2 and WS_2 monolayers. *ACS Nano* **2015**, *9*, 11658−11666.
(24) Napoleonov, B.; Petrova, D.; Minev, N.; Rafailov, P.; Videva, V.; Karashanova, D.; Ranguelov, B.; Atanasova-Vladimirova, S.; Strijkova, V.; Dimov, D.; Dimitrov, D.; Marinova, V. Growth of monolayer MoS_2 flakes via close proximity re-evaporation. *Nanomaterials* **2024**, *14*, 1213.
(25) Durairaj, S.; Krishnamoorthy, P.; Raveendran, N.; Ryu, B. D.; Hong, C.-H.; Seo, T. H.; Chandramohan, S. Barrier-assisted vapor phase CVD of large-area MoS_2 monolayers with high spatial homogeneity. *Nanoscale Adv.* **2020**, *2*, 4106−4116.
(26) Singh, A.; Moun, M.; Singh, R. Effect of different precursors on CVD growth of molybdenum disulfide. *J. Alloys Compd.* **2019**, *782*, 772−779.
(27) Ling, X.; Lee, Y.-H.; Lin, Y.; Fang, W.; Yu, L.; Dresselhaus, M. S.; Kong, J. Role of the seeding promoter in MoS_2 growth by chemical vapor deposition. *Nano Lett.* **2014**, *14*, 464−472.
(28) Yang, P.; Yang, A.-G.; Chen, L.; Chen, J.; Zhang, Y.; Wang, H.; Hu, L.; Zhang, R.-J.; Liu, R.; Qu, X.-P.; Qiu, Z.-J.; Cong, C. Influence of seeding promoters on the properties of CVD grown monolayer molybdenum disulfide. *Nano Res.* **2019**, *12*, 823−827.
(29) Xiong, J.; Wu, Q.; Cai, X.; Zhu, Y.; Lin, G.; Li, C. Comparative study of sodium and potassium compounds as promoters for growth of monolayer MoS_2 with high crystal quality on SiO_2/Si substrate. *J. Phys. D Appl. Phys.* **2024**, *57*, 405105.
(30) Xie, S.; Xu, M.; Liang, T.; Huang, G.; Wang, S.; Xue, G.; Meng, N.; Xu, Y.; Chen, H.; Ma, X.; Yang, D. A high-quality round-shaped monolayer MoS_2 domain and its transformation. *Nanoscale* **2016**, *8*, 219−225.
(31) Cho, Y. J.; Sim, Y.; Lee, J.-H.; Hoang, N. T.; Seong, M.-J. Size and shape control of CVD-grown monolayer MoS_2. *Curr. Appl. Phys.* **2023**, *45*, 99−104.
(32) Ma, T.; Ren, W. C.; Zhang, X. Y.; Liu, Z. B.; Gao, Y.; Yin, L. C.; Ma, X. L.; Ding, F.; Cheng, H. M. Edge-controlled growth and kinetics of single-crystal graphene domains by chemical vapor deposition. *Proc. Natl. Acad. Sci. U.S.A.* **2013**, *110*, 20386−20391.
(33) Kong, X.; Fu, C.; Gladkikh, V.; Ding, F. The shapes of synthesized two-dimensional materials. *SmartMat* **2023**, *4*, No. e1152.
(34) Sun, Y.; Wang, D.; Shuai, Z. Indirect-to-direct band gap crossover in few-layer transition metal dichalcogenides: a theoretical prediction. *J. Phys. Chem. C* **2016**, *120*, 21866−21870.
(35) Mak, K. F.; Lee, C.; Hone, J.; Shan, J.; Heinz, T. F. Atomically thin MoS_2: a new direct-gap semiconductor. *Phys. Rev. Lett.* **2010**, *105*, 136805.
(36) Mak, K. F.; He, K.; Lee, C.; Lee, G. H.; Hone, J.; Heinz, T. F.; Shan, J. Tightly bound trions in monolayer MoS_2. *Nat. Mater.* **2013**, *12*, 207−211.
(37) Xu, Z.; Lv, Y.; Li, J.; Wei, G.; Zhao, S. Pattern stimulated CVD growth of 2D MoS_2. *ChemistrySelect* **2020**, *5*, 6709−6714.
(38) Xu, D.; Lu, J.; Lin, G.; Zheng, M.; Chen, Y.; Miao, G.; Zhou, Y.; Cai, W.; Zhang, Y.; Wang, Y.; Zhang, X. Low-temperature synthesis of uniform monolayer molybdenum disulfide films. *Appl. Phys. Lett.* **2024**, *124*, 033101.

NOTE ADDED AFTER ASAP PUBLICATION

After this article was published ASAP April 16, 2025, corrections were made to Figure 9. The revised article was posted April 18, 2025.

https://doi.org/10.1021/acsomega.4c10312
ACS Omega 2025, 10, 16257−16264